

PAPER

Ensembles of novelty detection classifiers for structural health monitoring using guided waves


To cite this article: Gerges Dib *et al* 2018 *Smart Mater. Struct.* **27** 015003

View the [article online](#) for updates and enhancements.

Related content

- [An optimal baseline selection methodology for data-driven damage detection and temperature compensation in acousto-ultrasonics](#)
M-A Torres-Arredondo, Julián Sierra-Pérez and Guénaél Cabanes
- [Damage localization in metallic plate structures using edge-reflected lamb waves](#)
A Ebrahimkhanlou, B Dubuc and S Salamone
- [Adaptive high learning rate probabilistic disruption predictors from scratch for the next generation of tokamaks](#)
J. Vega, A. Murari, S. Dormido-Canto et al.

Ensembles of novelty detection classifiers for structural health monitoring using guided waves

Gerges Dib¹ , Oleksii Karpenko², Ermias Koricho³, Anton Khomenko⁴, Mahmoodul Haq⁵ and Lalita Udpa²

¹ Pacific Northwest National Laboratory, Richland, WA 99354, United States of America

² Department of Electrical and Computer Engineering, Michigan State University, East Lansing, MI 48824, United States of America

³ Department of Mechanical Engineering, Georgia Southern University, Statesboro, GA 30458, United States of America

⁴ General Photonics Corporation, Chino, CA 91710, United States of America

⁵ Composite Vehicle Research Center, Michigan State University, East Lansing, MI 48824, United States of America

E-mail: gerges.dib@pnnl.gov

Received 6 September 2017, revised 24 October 2017

Accepted for publication 31 October 2017

Published 17 November 2017



Abstract

Guided wave structural health monitoring uses sparse sensor networks embedded in sophisticated structures for defect detection and characterization. The biggest challenge of those sensor networks is developing robust techniques for reliable damage detection under changing environmental and operating conditions (EOC). To address this challenge, we develop a novelty classifier for damage detection based on one class support vector machines. We identify appropriate features for damage detection and introduce a feature aggregation method which quadratically increases the number of available training observations. We adopt a two-level voting scheme by using an ensemble of classifiers and predictions. Each classifier is trained on a different segment of the guided wave signal, and each classifier makes an ensemble of predictions based on a single observation. Using this approach, the classifier can be trained using a small number of baseline signals. We study the performance using Monte-Carlo simulations of an analytical model and data from impact damage experiments on a glass fiber composite plate. We also demonstrate the classifier performance using two types of baseline signals: fixed and rolling baseline training set. The former requires prior knowledge of baseline signals from all EOC, while the latter does not and leverages the fact that EOC vary slowly over time and can be modeled as a Gaussian process.

Keywords: guided waves, structural health monitoring, support vector machines, environmental and operating conditions, classification, novelty detection

(Some figures may appear in colour only in the online journal)

1. Introduction

Sparse sensor networks for guided wave structural health monitoring (GW-SHM) have been shown to be capable of damage detection using a small number of sensors [1–4]. Ultrasonic guided waves travel along the surfaces of solids which makes them efficient at inspecting large volumes using

sparsely spaced sensors. In GW-SHM sensor networks, one sensor transmits a pulse which travels through the structure and all other sensors in the vicinity listen to this pulse and process it for detecting damage signatures. This process is repeated periodically for continuously monitoring the structure's integrity. Due to low frequencies used for guided waves and the large spacing between sensors, received signals are

densely scattered from benign structural features such as edges, stiffeners and bolt holes. This results in complex superposition between benign structural scattering (we will also refer to this as baseline scattering) and defect scattering. To isolate the defect scattering, we need to estimate the baseline signal.

Uncertainties due to varying environmental and operating conditions (EOC) have been a limiting factor in the reliability of GW-SHM [5]. Those uncertainties are due to changes in temperature, humidity, and loading conditions on a structure, all of which affect the propagation properties of guided waves. Changes in wave amplitude and phase due to EOC can be mistaken for the presence of a defect, increasing false alarm rates.

Since nature is random, variations in EOC have a random nature. As a result, we can think of every guided wave measurement to be sampled from some unknown probability distribution. If we can determine the distribution of signals representing the structure's 'healthy' and 'damaged' states, we can construct optimal decision boundaries that maximize sensor network reliability.

There are infinite possible damage states, and it is only practical to obtain training data representing the structure's healthy state. We propose the use of a novelty classifier based on one class support vector machines [6] for enabling highly flexible damage detection and classification. This classifier learns the distribution of signals representing the healthy state of structure by training it using baseline signals only. Then, under the premise that defect signals are sampled from a different distribution, any signal outside the learned distribution represents a defect signal. The contributions of this paper are as follows:

- We identify appropriate features of narrow-band guided wave signals based on an analytical model. We introduce ensembles of novelty classifiers that are trained on different segments of the guided wave signal. For each classifier, an ensemble of predictions are made for a received signal.
- We develop a multiplicative feature aggregator which transforms high dimensional guided wave signals onto a two-dimensional subspace, while at the same time quadratically increasing the number of available observations for training.
- We introduce the concept that EOC effects follow a Gaussian process model, and propose using a rolling baseline training set as opposed to a fixed and pre-recorded baseline set.
- Extensive analytical simulations which demonstrate the performance of the classifier under different levels of EOC severity. This shows expected behavior of the classifier in different environments (e.g. water loading) without the need to collect experimental measurements.
- We provide the classifier performance for impact damage detection using experiments on composite plates under small variations in temperature. We also study the effects of different number of baseline signals for both the fixed and rolling baseline set approaches.

2. Related work

Several methods have been proposed in the literature to deal with EOC variations and uncertainties without the need to explicitly measure them. Research has focused on temperature variations, because it has been claimed to have the largest effect on guided wave signals. For example, Konstantinidis *et al* [7] has shown that coherent noise was present between measurements taken only 5 min apart. The simplest and perhaps the most common method used to deal with uncertainties is optimal baseline selection (OBS) [2]. In this method, a set of baseline signals is collected at different temperatures. When a new signal is received, an optimal baseline is selected based on minimizing the mean square error. Then, the signal scatter is computed by subtracting a corrected version of the selected baseline from the current signal. In this paper, we do not attempt to select a particular baseline signal, rather, we use all available baseline signals to train the classifier. Another common method, which is often used in conjunction with OBS is the baseline signal stretch where several variants have been proposed [8–10]. This method stretches the baseline signals in time to minimize a cost function relative to a received signal.

GW-SHM has been shown to be capable of detecting damage in both metals and composite materials. Dib *et al* [11, 12] have shown the feasibility of using guided waves for impact damage detection in composite plates. Liu and Chattopadhyay [13] investigated different guided wave features for detecting impact damage in a sandwich composite wing. A total of nine features in the time and frequency domains were selected, and dimensionality reduction methods were used to cluster the results into damaged and non-damaged clusters. Hayes *et al* [14] investigated multiple guided wave signal features and data fusion schemes using data from a bolted-frame and a fuselage rib structure. Other techniques have involved dimensionality reduction using principal component analysis and then using clustering methods, hypothesis testing or statistical analysis for classification [15–18].

As for developing techniques for acquiring baseline data, Putkis and Croxford [19] proposed a continuously growing baseline method for mitigating environmental change effects. We use ideas similar to those proposed in [19], where the training baseline set does not need to be known apriori. This paper presents a method that uses all available baseline signals to train the classifier. We introduce the concept of modeling the effects of EOC variations as Gaussian processes, and a rolling window of baseline sets for continuous training-prediction cycles of the classifier.

3. Damage detection procedure

We first introduce the terminology, notation and conventions used in this paper. A vector is represented by a boldface lower case letter. A tilde over the vector \tilde{s} indicates a vector of complex numbers. Since we are dealing with digital signals, $\tilde{s}[n]$ denotes the digital samples of the complex signal \tilde{s} . We

also interpret $\tilde{s}[n]$ to be the n th component of the vector $\tilde{\mathbf{s}}$. We will use the vector notation or the digital signal notation interchangeably depending on context and convenience.

Consider a single actuator-sensor path within a sensor network. The actuator transmits a band-limited pulse of duration T seconds and a center frequency ω_c . We represent the transmitted pulse in discrete time as a complex signal:

$$\tilde{s}[n] = \begin{cases} w[n] \exp[j\omega_c n] & \text{if } 0 \leq n \leq T f_s \\ 0 & \text{otherwise,} \end{cases} \quad (1)$$

where f_s is the sampling frequency; $w[n]$ is a pulse shaping window function with unit power (i.e. $\mathbf{w}^T \mathbf{w} = 1$). In a dense structural scattering environment, the transmitted signal is attenuated, shifted and delayed before arriving at the receiver. When a defect is also present in the structure, the received signal is the superposition of P scattered echoes from benign structural discontinuities and Q scattered echoes from damaged related discontinuities, and can be expressed as:

$$\tilde{r}[n] = \underbrace{\sum_{p=1}^P \tilde{\alpha}_p w[n - \tau_p] \exp[j\omega_c(n - \tau_p)]}_{\text{baseline}} + \underbrace{\sum_{q=1}^Q \tilde{\beta}_q w[n - \tau_q] \exp[j\omega_c(n - \tau_q)]}_{\text{defect}}, \quad (2)$$

where $(\tilde{\alpha}_p, \tau_p)$ and $(\tilde{\beta}_q, \tau_q)$ are the complex attenuation and time delay of the structural and defect echoes, respectively. Given the received signal, the objective is to classify the structure as ‘healthy’ or ‘damaged’. This is equivalent to determining if the defect term in equation (2) exists. The challenges with this classification problem are two fold:

- (1) The baseline and defect terms in equation (2) have the same sinusoidal form. Thus, recovering the defect signal requires the exact baseline signal.
- (2) Environmental and operating conditions result in variations and randomness in the baseline signal in equation (2). Thus subtraction by a previously measured baseline signal will contain some random error.

It is often possible to obtain a collection of baseline signals spanning the space or subspace representing the ‘healthy’ structure, within the current structure’s EOC. Given a set of M baseline signals, our goal is to learn a classifier function $f: \mathbb{R}^D \rightarrow \{-1, +1\}$ which is a mapping from D dimensional feature space to -1 for a ‘damaged’ structure and $+1$ for a ‘healthy’ structure. In the following, we will first describe the mapping function to obtain the signal features in order to reduce the high dimensional time signal to a smaller dimension D . The procedure used to learn the function f , and its use to obtain a final decision is also discussed.

3.1. Feature selection

Dense scattering of guided waves results in a received signal with delay profile much larger than the transmitted wave pulse width, i.e. $\max_{p=\{1 \dots P\}} \tau_p \gg T$. This large delay spread results in frequency selective fading in the signal’s power spectrum [20]. Even the smallest change in EOC might result in significant change in the signal’s power spectrum. To

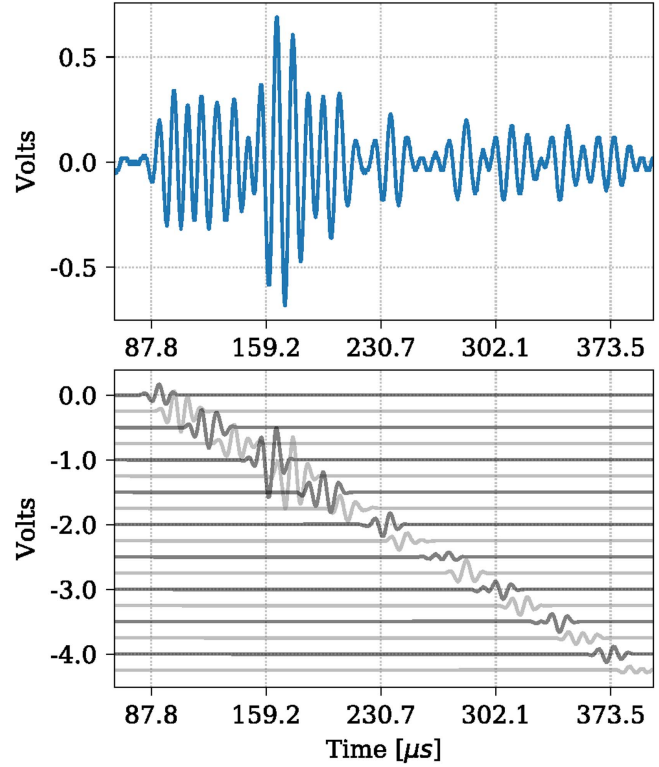


Figure 1. A typical guided wave signal (top) segmented into independent processing time bins (bottom). The time bins are allowed to have a 50% overlap.

mitigate this phenomenon, we segment the received signal into L time bins each of length equal to $N = T f_s$. This signal segmentation is demonstrated in figure 1. The signal within each time bin $l \in \{1 \dots L\}$ is defined as $\tilde{r}_l[n] = w[n - Nl] \tilde{r}[n]$ where $\tilde{r}[n]$ is defined in equation (2), and $w[n]$ is the window function defined in equation (1). In addition to enhancing the signal’s spectral properties, segmentation provides multiple channels over which we can independently train an ensemble of classifiers, as we will describe in the next section.

For each time bin, we compute the Fourier transform of the signal at the excitation frequency ω_c :

$$\tilde{R}_l = \mathcal{F}(\tilde{\mathbf{r}}_l; \omega_c) \quad (3)$$

and the feature vector is constructed from the real and imaginary parts of equation (3):

$$\mathbf{F}_l = [\text{Re}(\tilde{R}_l), \text{Imag}(\tilde{R}_l)] \quad (4)$$

this is effectively the same as the amplitude and phase of the signal within the l th time bin. The rationale for selecting these features is that the echoes of the baseline portion in equation (2) are completely specified by the attenuation coefficients $\tilde{\alpha}_p$ and time delays τ_p . However, within a given time bin, the time delays of multiple echoes are small, and thus the baseline portion is specified by some effective attenuation coefficient $\tilde{\alpha}$, which is recovered by the Fourier transform.

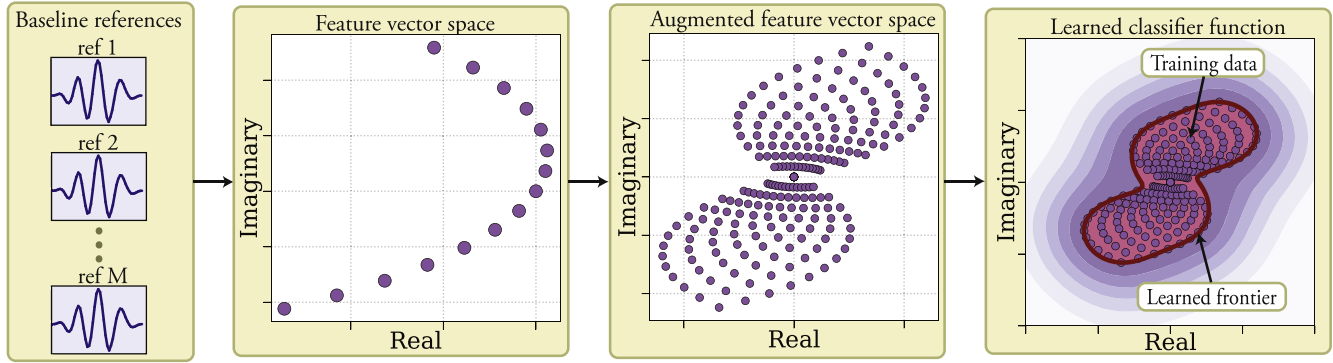


Figure 2. Overview of the learning approach for each time bin, which has three parts (1) transform the high dimensional baseline reference signals into a 2D feature space (the complex plane); (2) feature augmentation which represents the error distribution by computing the distances between all the points in the feature vector space; and (3) learning the frontier for the error region using one class SVM.

We have now reduced a received signal $\tilde{\mathbf{r}}$ from NL dimensions into a set of L feature vectors, each of which is two dimensional ($D = 2$).

3.2. Learning approach

The classifier is trained to learn an independent function mapping for each of the L time bins. The approach is shown in figure 2 for a particular time bin l , knowing that the same procedure is repeated for all L time bins. We describe the procedure as follows:

3.2.1. Feature vector space mapping. For each of the M baseline signals, compute the feature vector as given in equation (4), resulting in a design matrix of dimensions $M \times 2$. Note that the design matrix columns represent different features, and its rows represent different observations.

3.2.2. Feature augmentation. Subtract each row of the current design matrix from all the rows of the same design matrix. This results in a new design matrix with size $M^2 \times 2$, thus augmenting the number of training data quadratically relative to the number of available baseline signals. This subtraction transforms the design matrix from being a representation of the baseline signal distribution to a representation of the error distribution due to EOC. This data augmentation represents the error distribution because if the m th baseline represents a received signal from a healthy structure, then its distance from all the other baseline signals spans the space of possible residual errors.

3.2.3. Classifier learning. Since our design matrix contains training data from only one class, we have an unsupervised classification problem. This is equivalent to a novelty detection task, where we learn a function f which returns $+1$ if a vector lies within the space spanned by the training data, and -1 otherwise. A flexible and efficient method for this type of novelty detection is one class support vector machine method (OCSVM) [6]. We propose using the radial basis function (RBF) to learn complex functions such as the frontier shown in figure 2. Training OCSVM with RBF kernel

requires the specification of two hyper-parameters: (i) the bandwidth for the RBF kernel γ ; and (ii) the regularization coefficient ν .

To specify those two hyper-parameters, we perform a randomized grid search using cross-validation, such as leave one out cross validation [21], where the goal is to minimize the false alarm rate, or achieve a maximum allowable false alarm rate. An important point to consider during cross-validation is retaining the coverage of baseline signals used for the training split, especially when the baseline signals represent particular environmental conditions. For example, if one baseline signal is available for every 2°C change in temperature over a known operating range, then K fold cross-validation might not be the best approach since the training split would not cover the operating temperature extremes.

General guidelines dictate giving ν a small value (<0.1) and $\gamma \in [0.05, 0.6]$ for standardized (i.e. the observations have zero mean and unit standard deviation) training data. To prevent overfitting, smaller values of γ are recommended when a small number of baselines is available.

3.3. Classification approach

The classification task makes a damage/no damage decision, given a received signal $\tilde{\mathbf{r}}$. Figure 3 shows the classification approach for a given time bin. We describe the procedure as follows:

3.3.1. Feature vector space mapping. The received signal within a time bin $\tilde{\mathbf{r}}_1$ is mapped onto feature space using equation (4). The same is done for each of the available M baseline reference signals. Then, the difference between the received signal feature vector and the M baseline reference feature vectors is computed, resulting in a total of M feature vectors.

3.3.2. Feature vectors classification. For each of the M feature vectors, we use the trained OCSVM to provide the classification into $\{-1, +1\}$, where -1 indicates that the point is outside the learned frontier (defect) and $+1$ indicates

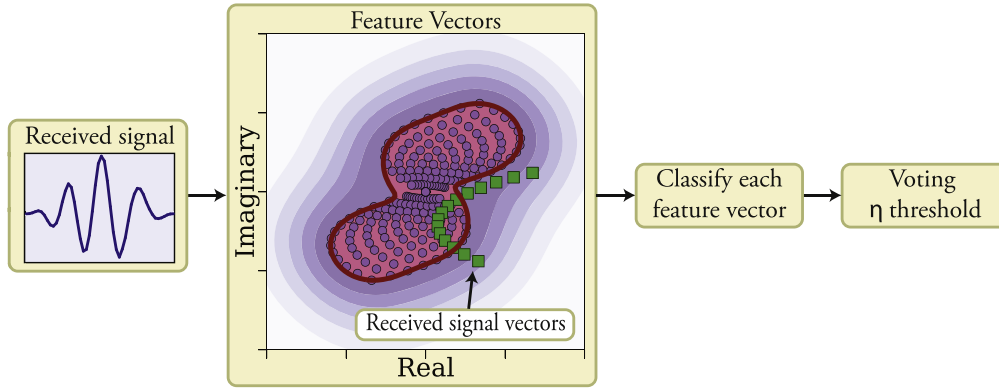


Figure 3. Overview of the classification approach for a given time bin, which has three parts: (1) the received signal is transformed to feature space, and then subtracted from each of the M baseline feature vectors; (2) each of the M received signal feature vectors is classified +1, -1, depending if it lies within the learned frontier or not; (3) use a voting scheme to make a final decision, where at least a fraction η of the M vectors could be classified as +1 before making a +1 final decision.

it is inside the learned frontier (no defect). This gives us a total of M decisions.

3.3.3. Single classifier voting. Using the M decision, we need a voting scheme to make a final decision using the classifier for this time bin. To do this voting, we define a threshold $\eta \in (0, 1]$. If the fraction of decisions with value +1 is greater than η , then we decide 'no damage', otherwise the received signal is classified as 'damaged'.

3.3.4. Ensemble voting. So far we have obtained L decisions from each of L classifier; one for each time bin. Again, we need a voting scheme to make a final decision based on the ensemble of classifiers. In this case, we introduce another threshold $\zeta \in (0, 1]$, which is the minimum fraction of classifiers with a decision of +1, before deciding that the structure is healthy.

The thresholds η and ζ are two hyper-parameters that need to be specified. We combine those two parameters with the OCSVM hyper-parameters and make a 4 parameter randomized grid search using cross validation as described in the previous section. As a general guideline, we set η and ζ to be greater than 0.5, unless we have a small number of baselines (less than 5). If the extent of environmental changes is not represented by the available baseline references, then we can let η or ζ to be less than 0.5 to reduce the false alarm rate.

It is worthwhile to note that EOC effects will be more severe at later time bins within a guided wave signal, possibly resulting in consistently better performance for the classifiers from earlier time bins. To mitigate the effects of this phenomenon, weighted voting can be used, where classifiers at earlier time bins will have higher weights than those at later time bins.

4. Theoretical analysis

This section describes the use of analytical reasoning and Monte-Carlo simulations based on simplifications of

equation (2) to study the behavior of the proposed classifier under effects of EOC and baseline coverage. By baseline coverage we mean the extent to which the baseline signals used in training the classifier represent all possible EOC.

Consider a received signal with a single time bin. For convenience, we will drop the l subscript which indicates the time bin number. If there is only the direct wave path and a single damage echo (i.e. $P = 1$ and $Q = 1$ in equation (2)), the received signal becomes:

$$\tilde{r}[n] = \tilde{\alpha}_p w[n - \tau_p] w[n] \exp[j\omega_c(n - \tau_p)] + \tilde{\beta}_q w[n - \tau_q] w[n] \exp[j\omega_c(n - \tau_q)]. \quad (5)$$

Computing the Fourier transform at the frequency ω_c we obtain:

$$\tilde{R} = \tilde{\alpha}'_p \mathbf{w}_{\tau_p}^T \mathbf{w} + \tilde{\beta}'_q \mathbf{w}_{\tau_q}^T \mathbf{w}, \quad (6)$$

where we have adopted the notation that \mathbf{w}_{τ_p} is the vector with components $w[n - \tau_p]$, and $\tilde{\alpha}'_p = \tilde{\alpha}_p \exp[-j\omega_c \tau_p]$. The same goes for the defect terms. Note that since we defined the window function \mathbf{w} to have unit power, then $0 \leq \mathbf{w}_{\tau_p}^T \mathbf{w} \leq 1$ is the correlation coefficient between the envelop of received signal's baseline portion and the window function. Since $\mathbf{w}_{\tau_p}^T \mathbf{w}$ is a real scalar, we further simplify equation (6):

$$\begin{aligned} \tilde{R} &= \tilde{\alpha}''_p + \tilde{\beta}''_q \\ &= |\tilde{\alpha}''_p| \exp[j\angle \tilde{\alpha}''_p] + |\tilde{\beta}''_q| \exp[j\angle \tilde{\beta}''_q], \end{aligned} \quad (7)$$

where $\tilde{\alpha}''_p = \tilde{\alpha}'_p \mathbf{w}_{\tau_p}^T \mathbf{w}$, and similarly for the defect terms. Under varying EOC, the variations in the signal feature are reflected by changes in the baseline portion of equation (7). In the following, we will use Monte-Carlo simulations, where we model the baseline portion of equation (7) as a Gaussian process, while the defect portion is kept deterministic. The Monte-Carlo simulations will be used to evaluate the reliability of damage detection under varying EOC conditions, which are reflected in the range of $|\tilde{\alpha}''_p|$ and $\angle \tilde{\alpha}''_p$.

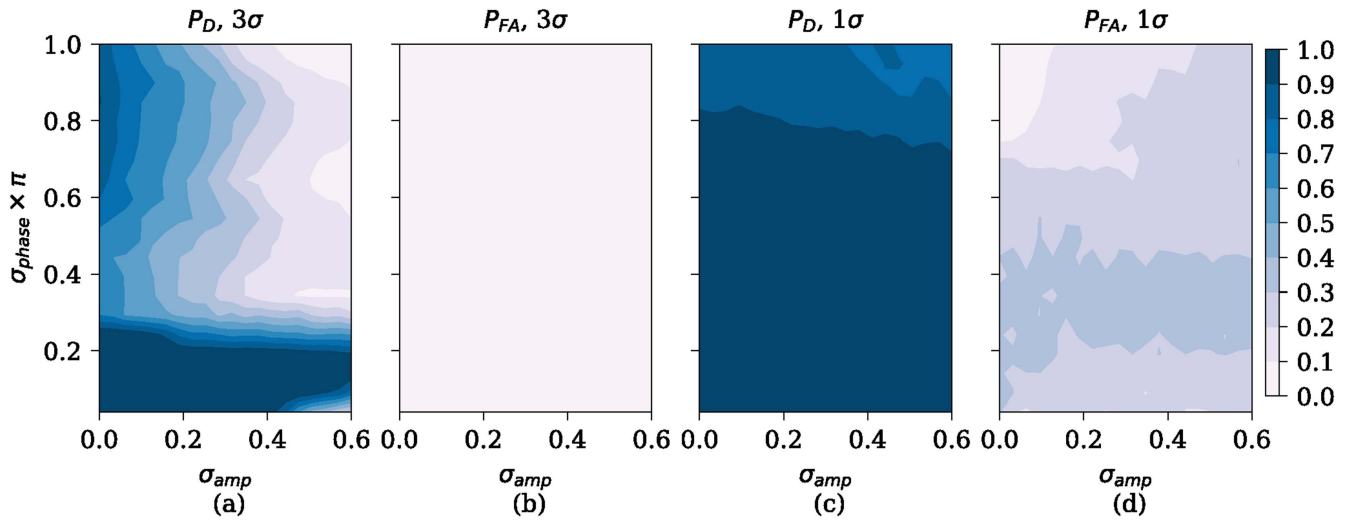


Figure 4. Effects of EOC extent of variation and baseline coverage on probability of false alarm and probability of detection. The x -axes represent the standard deviation of signal's amplitude and the y -axes represent the standard deviations dues of signal's phases. The two plots from the left show performance results when the baseline signals cover 3σ of the total variation (i.e. about 99% of the extremes due to varying EOC). The right two plots show the performance results when the baseline signals cover σ variation (i.e. about 34% of the extremes due to varying EOC).

4.1. Fixed Baseline References

In this scenario, we have a fixed set of pre-recorded M baseline reference signals which are used to train the classifier. To achieve a reliable performance, it is desired that the baseline reference set represent all possible EOC that the structure might be subjected to. Since EOC can vary randomly, the amplitude and phase of the baseline portion of equation (7) will also be random.

To assess how the proposed classifier works under different severity levels of EOC's, we model the baseline portion of the received signal feature vector to be sampled from a two dimensional independent and identically distributed Gaussian process:

$$\begin{bmatrix} |\tilde{\alpha}_p''| \\ \angle \tilde{\alpha}_p'' \end{bmatrix} \sim \mathcal{N} \left(\begin{bmatrix} 1 \\ 0 \end{bmatrix}, \begin{bmatrix} \sigma_{\text{amp}}^2 & \rho \sigma_{\text{amp}} \sigma_{\text{phase}} \\ \rho \sigma_{\text{amp}} \sigma_{\text{phase}} & \sigma_{\text{phase}}^2 \end{bmatrix} \right), \quad (8)$$

where σ_{amp}^2 is the variance in the baseline amplitude, σ_{phase}^2 is the variance in the baseline phase, and ρ is the cross-correlation between the baseline amplitude and phase. A large value for σ_{phase}^2 and/or σ_{amp}^2 indicates large variations in EOC. The mean baseline signal amplitude is 1 and the mean phase is 0. We let the defect portion in equation (7) to be a deterministic value for a given defect shape and width.

In figure 4 we show the performance in terms of probability of detection and false alarm rate under different values of σ_{amp} and σ_{phase} . The classifier was trained using a set of 20 baseline signals, and the hyper-parameters were set as ($\gamma = 0.05$, $\nu = 0.01$, $\eta = 0.8$). In all simulations, the defect signal was fixed such that $\tilde{\beta}_q'' = 2 \exp[j\pi]$.

Figures 4(a) and (b) show the case when the baseline references have good coverage. Their amplitudes span the range $1 \pm 3\sigma_{\text{amp}}$ and phases span the range over $\pm 3\sigma_{\text{phase}}$. In this case, the false alarm probability (figure 4(b)) is largely constant and less than 10% for all EOC conditions. On the

other hand, the probability of detection (figure 4(a)) decreases with increasing EOC severity (high σ_{phase} and σ_{amp}). Good performance may be achieved for small phase variations in the received signal, up to $\pi/5$, and large amplitude variations up to 40%.

The case when the baseline references do not have good coverage is shown figures 4(c) and (d). The baseline reference amplitudes span the range $1 \pm \sigma_{\text{amp}}$ and phase spans the range $\pm \sigma_{\text{phase}}$. In this case we obtain a probability of detection over 90% even for large EOC variations, but the performance decreases as the phase variations increase. On the other hand, the probability of false alarm increases to 20%–40% for most EOC conditions. It is important to note that the probability of false alarm decreases for severe EOC conditions. This is, however, expected, since large fluctuations in EOC result in larger signal variations, which then decreases the chance that SVM would overfit the baseline data. However, this situation also reduces the probability of detection rates.

4.2. Rolling baseline references

Up to this point, we have assumed that the M baseline references are pre-recorded. However, this is often not necessary, and baseline references can be collected while the structure is in operation. In practice, EOC's change slowly over time, thus it is expected that the guided wave signals will also vary slowly over time. Based on this observation, we can continuously update the available baseline signals using a rolling slow time window. Slow time represents the time scale of data collection, and is typically seconds, minutes, or hours. This is in contrast to fast time which is the time required to sample a guided wave signal and is typically on the scale of microseconds. At a given instant of time t , we retain only M latest signals and use them to re-train the classifier. The newly trained classifier is used to classify the signal at the current time instant t .

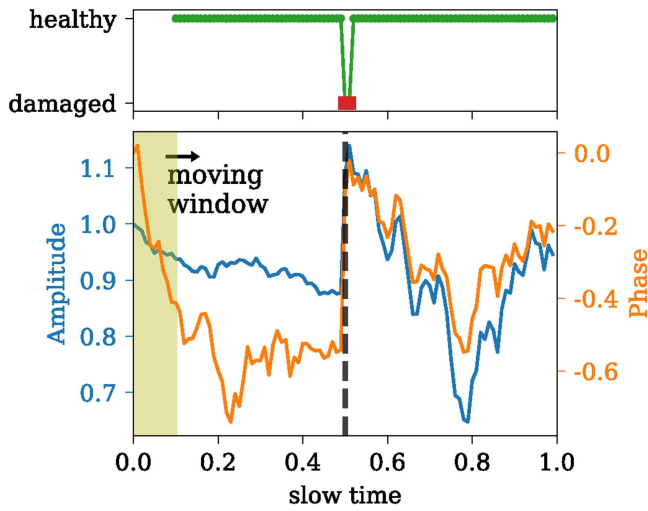


Figure 5. The bottom plot shows the amplitude and phase of received signal, which follow a Gaussian process with a Brownian motion kernel. The vertical dashed line at time 0.5 indicates the time that a damage was introduced. The shaded region shows the portion of slow time within which recored signals are used as baseline references. The top plot shows the decision of the classifier as the window moves in slow time.

To demonstrate this effect, we simulate the slow variations in baseline signal's amplitude and phase using a multi-dimensional Gaussian process, as shown in figure 5. Unlike the simulations used for the fixed baseline set case, we do not have the independent and identically distributed assumption, and we allow the received signal feature vectors to be correlated in slow time. We use a Brownian motion kernel [22] to define the covariance matrix of the received signals in slow time:

$$k(\tilde{\mathbf{r}}(t), \tilde{\mathbf{r}}(t - \tau)) = \sigma^2 \min(\tilde{\mathbf{r}}(t), \tilde{\mathbf{r}}(t - \tau)), \quad (9)$$

where t represents the slow time, and τ the slow time difference between two received signals. σ^2 is the feature variance which is σ_{amp}^2 for the amplitude, and σ_{phase}^2 for the phase. Note that the phase and amplitude are correlated as given by equation (8). In figure 5, we set $\sigma_{\text{amp}} = 0.1$, $\sigma_{\text{phase}} = \pi/5$, $\rho = 0.5$, and the moving window size to be such that 10 baseline references are available at each time instant. The classifier hyper-parameters are set to ($\gamma = 0.2$, $\nu = 0.01$, $\eta = 0.2$), and the defect signal is set to $\tilde{\beta}_q'' = 0.5 \exp[j\pi/4]$. Figure 5 (top) shows the classifier decision at each time instant. The classifier provides the correct decision at the instant damage is introduced, and quickly resets after that where the damaged structure is now considered the new 'healthy state'. This is because the baseline reference window evolves with time, and uses the signals from the detected defect to re-train the classifier.

An important aspect of the reliability of rolling classifiers is the window size relative to coherence in slow time; the distance in time between two received signals to be considered uncorrelated. If the window size is too small relative to slow time coherence, then the classifier will not be able to capture variations due to EOC and it will overfit the baseline data. In this context, overfitting can be thought of as a tighter

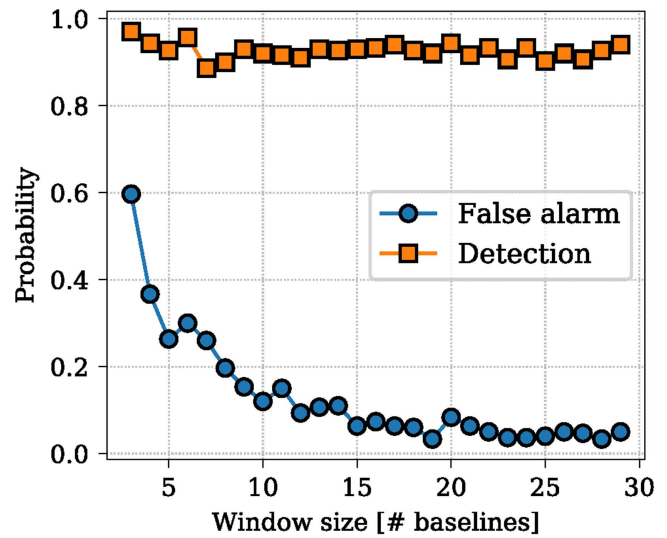


Figure 6. Effect of changing the window size (or number of baseline references) for the rolling classifier on the probability of false alarm and probability of detection.

learned frontier as depicted in figure 2. The effect of window size on probability of detection and false alarm rate is shown in figure 6. The probability of detection stays mostly unchanged for all window sizes. This indicates that the simulated flaw response is sufficiently far from the learned frontier. For smaller flaws, one expects the probability of detection to decrease with increasing window size, since the learned frontier will grow. On the other hand, the false alarm rate rapidly decreases as the window size is increased, since a larger learned frontier will cover more of the variations in EOC.

5. Experiments

We prepared an eight layer, 4.8 mm thick, glass fiber composite plate with plain-weave S-glass/SC-15 epoxy, and instrumented it with a total of seven circular PZT-5A transducers having 7 mm diameter and 0.2 mm thickness. The PZT transducers were bonded to the specimen surfaces using two-part epoxy adhesive with relative locations described in figure 7. One transducer (labeled 2T in figure 7) was used as the transmitter. The six other transducers were used as receivers. Three of the receivers were bonded to the impacted surface of the specimen (transducer names 4, 5, 6 suffixed by the letter 'T' in figure 7), and the other three receivers were bonded to the same locations, but on the opposite surface (labeled 'B').

The specimen was subjected to drop-weight impacts at its center according to ASTM D7136 standard. An Instron 9250 HV Dynatup impact machine was used, which is equipped with an 88.96 kN load cell impactor, a velocity detector, and a pneumatic brake to prevent multiple impacts. The specimen was clamped by pneumatically assisted grips, as shown in figure 8. The exposed diameter of the composite plate for impact loading was 76.2 mm. A 12.7 mm diameter

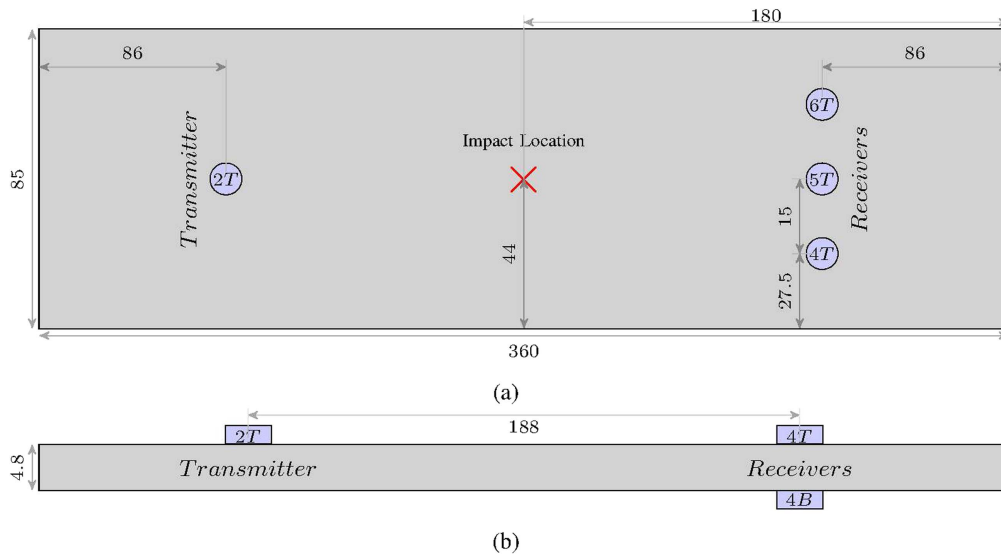


Figure 7. Schematic of the composite plate and the locations of the PZT transducers bonded to its surfaces. Three PZT receivers are bonded to the top surface and another three are bonded to the corresponding positions at the bottom surface. A single PZT transmitter is bonded to the top surface of the plate. (a) Top view of the plate, (b) side view. All dimensions are in millimeters.

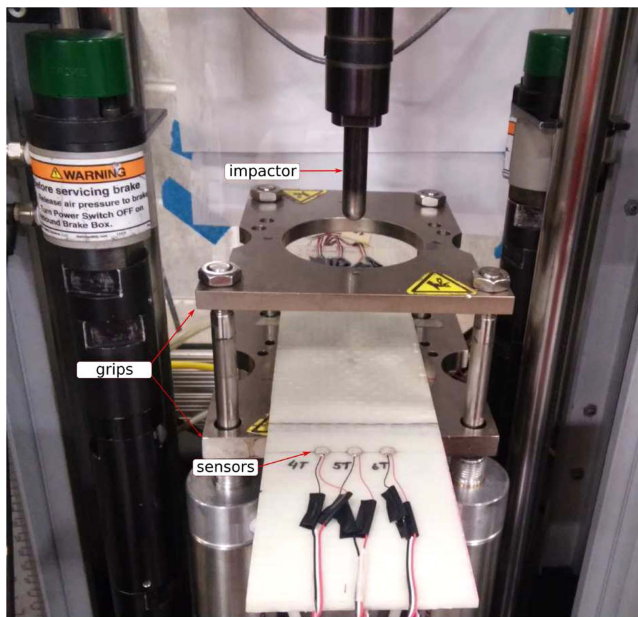


Figure 8. Glass fiber composite specimen with instrumented piezoelectric sensors clamped inside the Instron drop-weight impact machine.

hemispherical head impactor was used for the impact tests. The specimen was hit by a total of nine impacts with energies summarized in table 1. The first five impacts were all of the same energy, and then the remaining four impacts had increasing energy levels. Both optical scans and ultrasonic guided wave measurements were collected before any impact to obtain baseline data, and then after each impact. The procedures for the optical and ultrasonic guided wave measurements are described in the following sections.

Table 1. Energies used to impact the specimen.

Impact	Energy (J)
1	1.5
2	1.5
3	1.5
4	1.5
5	1.5
6	3.5
7	4.5
8	6.0
9	7.5

5.1. Optical measurements

A novel optical transmission (OT) scanning system was used for imaging the specimen after each impact in order to obtain detailed information about delamination area after each impact. A detailed description of this optical measurement system was reported in [23–25].

OT scans obtained from the specimen in its healthy state, and after each of the nine impacts are shown in figure 9. These scans only show the center region of the specimen, in the vicinity of the impacts location. The optical transmittance measurements are sensitive to thickness variations of the test specimen. Besides, resin-rich and fiber-rich areas can also be detected as be recognized by observing the baseline OT-scan. When delamination/fiber breaking is introduced within the specimen, the OT coefficient is reduced, resulting in a lower power registered at the receiver. Thus dark regions in figure 9 identify the delaminated area due to the impact. We quantify this delamination area using the following procedure:

- (1) *Normalization:* We normalized all the scans by their maximum value so that the pixel value ranges from 0 to 1.

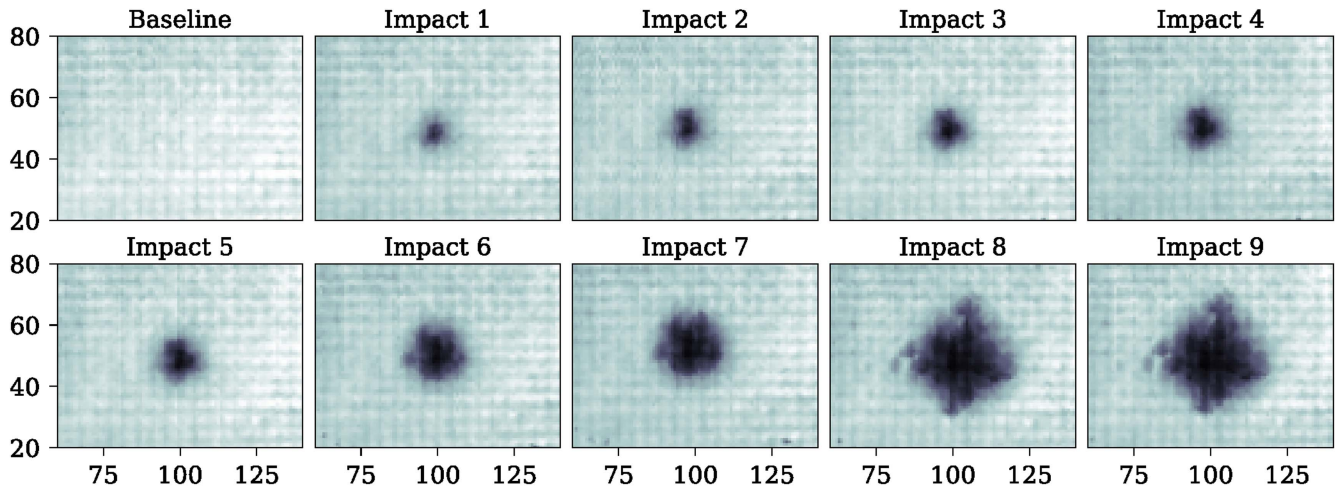


Figure 9. OT scans for the specimen in its pristine condition, and after each of the nine impacts. The axes coordinates are shown in millimeters.

- (2) *Threshold computation:* We use the baseline image to select the threshold. Since no delamination is present in this scan, then the variations of optical transmittance are due to non-uniform thickness and non-uniform distribution of fibers in the specimen [24]. Then, 75% of this minimum value is taken as threshold.
- (3) *Image thresholding:* We convert the OT scans into binary images using the computed threshold.
- (4) *Image closing:* Morphological closing on the binary image comprising of image dilation followed by an erosion. We used a 3×3 square window as the structuring element for morphological operations. This removes any isolated dark pixels, or closes up small gaps between bright pixels.
- (5) *Area computation:* The area of the delamination is the number of bright pixels scaled by the scan resolution.

The resulting delamination area computation after each impact is shown in figure 10. Impacts 1–5 are repeated impacts of same energy (see table 1), and the delamination area increases slowly after each impact. Then delamination area increases rapidly when the impact energy is increased from impacts 6–9.

5.2. Guided wave measurements

Guided wave measurements were collected when the specimen was in its healthy state and after each impact. PZT transducer 2T was used as transmitter. It was excited by a 100 kHz Gaussian modulated tone burst with 50% bandwidth and 18 V peak to peak. This frequency was selected because it provided good signal to noise ratio, and at the same time a long signal delay spread, so that classifier ensembles can be used on the multiple time bins. Transducers 4, 5, and 6 (top and bottom) were used as receivers connected to a custom build multi-channel charge amplifier providing high sensitivity and low noise measurements. The output from the charge amplifier was recorded by an oscilloscope. In addition to taking the measurements at room temperature, the specimen was put in an oven, and temperature was increased from

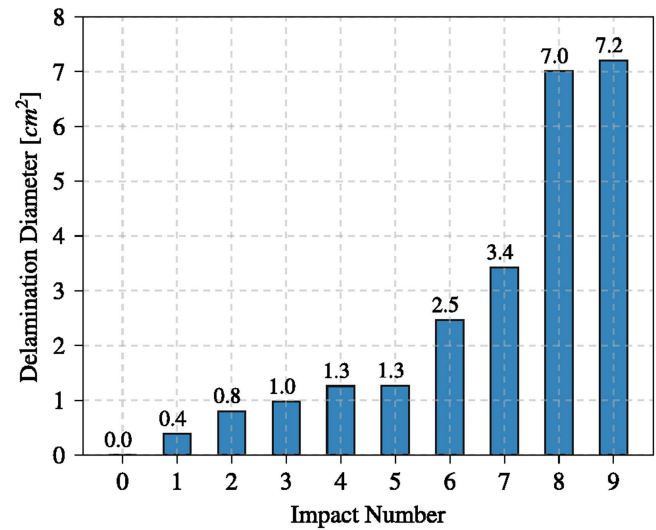


Figure 10. Computed total delamination area after each impact based on the OT scan images.

room temperature (approximately 22 °C–25 °C) up to 50 °C. Guided wave measurements were collected continuously as the specimen temperature was increased. We acquired approximately 20–24 signals at different temperatures for each damage state (number of signals differed for different damage states).

Figure 11 shows all the acquired baseline signals and the signals after impact 5 for each receiver. Temperature changes result in a change of the signal's time delay, consistent to what has been reported in the literature [2, 8, 9]. Also a change of amplitude is observed, which can be attributed to changes in the efficiency of piezoelectric transducers. Impact damage also results in a similar signal variation as seen in figure 11.

5.3. Results using fixed baseline references

A total of 24 baseline signals were obtained for temperatures ranging from 25 °C to 50 °C. We use multiple subsets of the

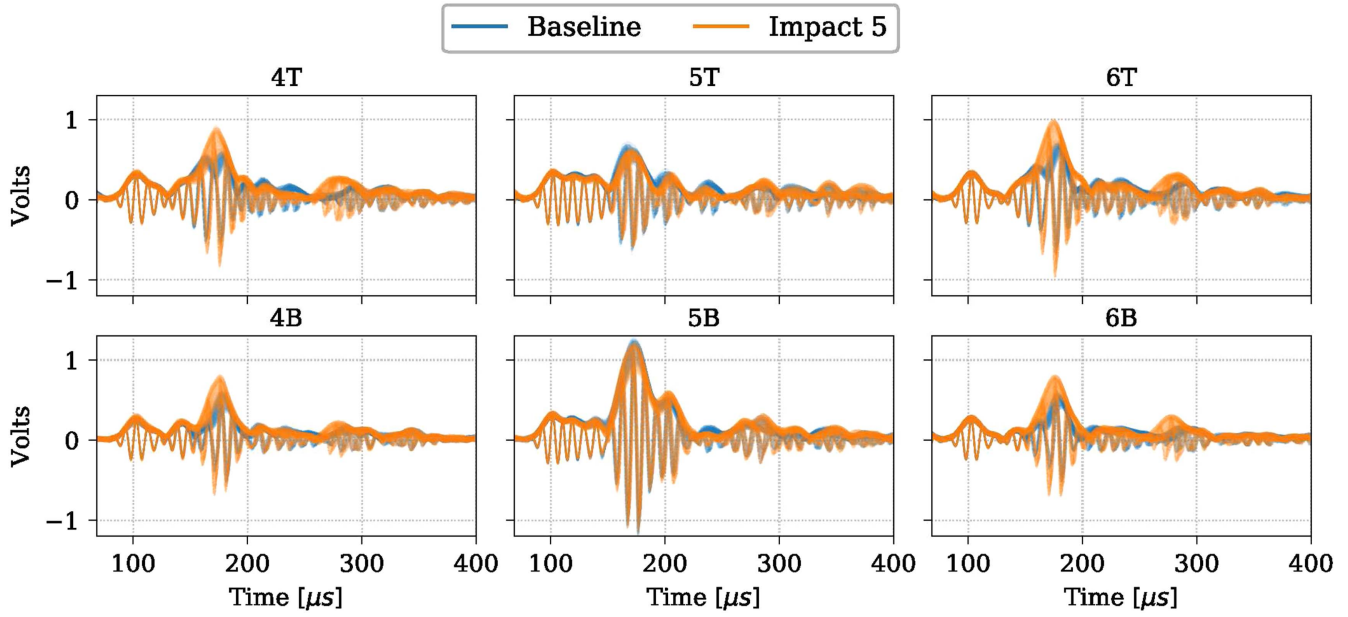


Figure 11. The received guided wave signals for each of the six receivers used in the experiments. For each receiver, we show all the recorded baseline signals and their envelopes, indicating the range of change in amplitude and phase of the signals due to temperature change. The same is also shown for signals collected after impact 5.

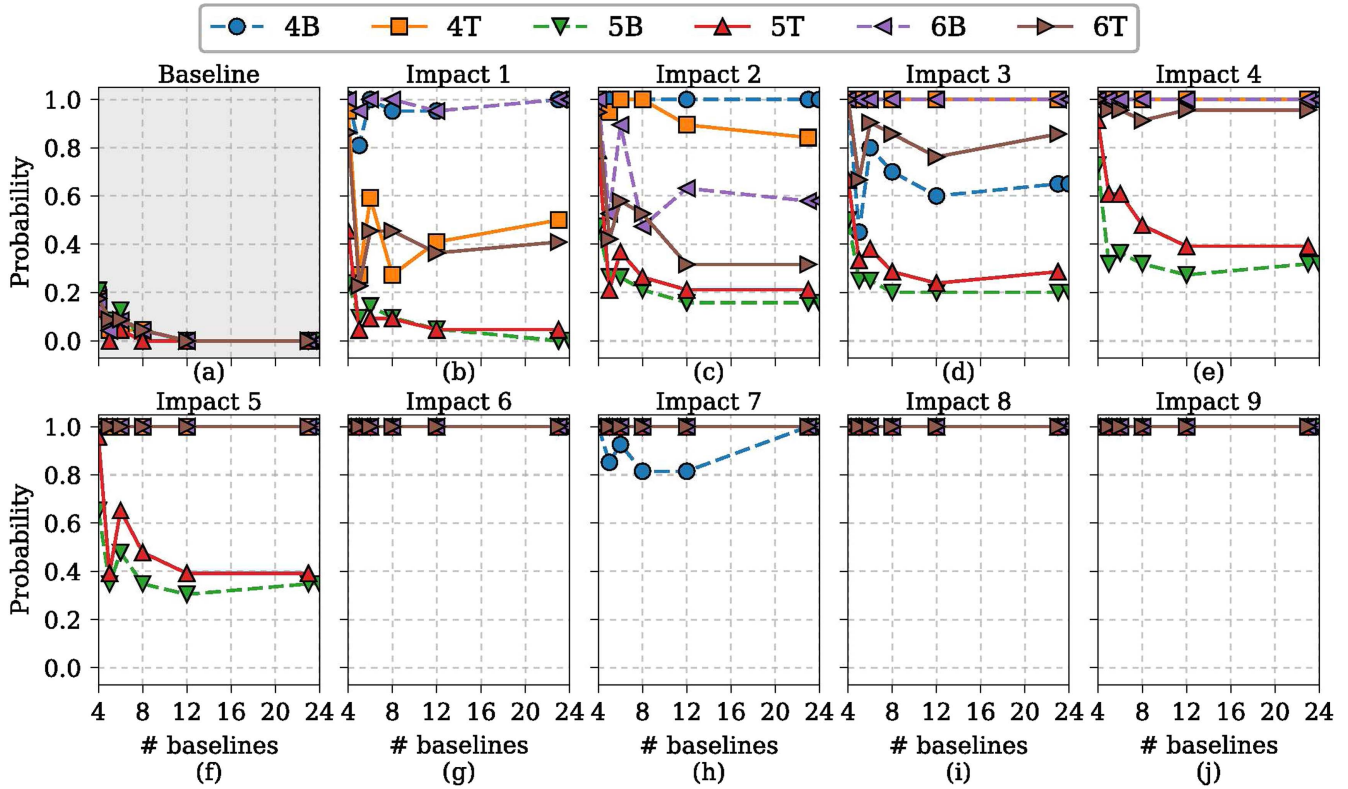


Figure 12. Probability of false alarm and probability of detection for each of the 6 receivers as a function of the number of baseline signals used to train the classifier. The upper left plot is shaded and shows the probability of false alarm. All the other plots show the probability of detection after each impact.

baseline signals varying from only 4 baselines up to all the 24 baselines to train the classifier. The baseline signals were selected so that they have a complete coverage (i.e. include

the minimum and maximum temperature). We set the classifier hyper-parameters to ($\gamma = 0.05$, $\nu = 0.01$, $\eta = 0.55$, $\zeta = 0.8$). The probability of false alarm is computed as

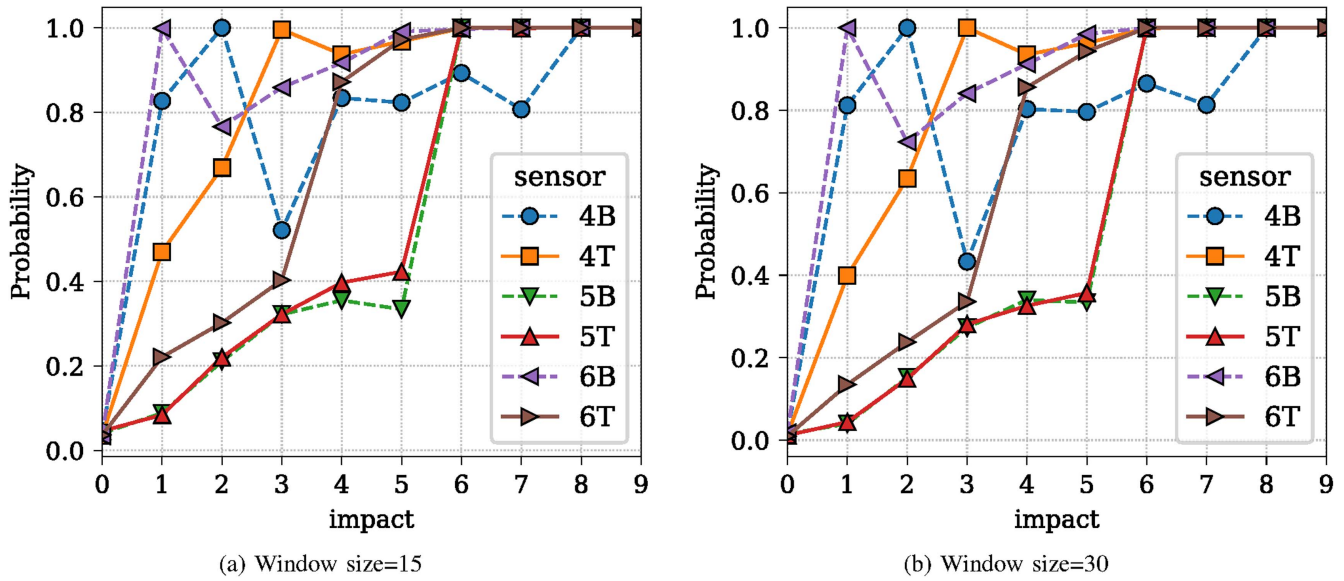


Figure 13. Probability of false alarms and detection of the rolling baseline classifier obtained under the virtual slow time for the experiment data. The probability of false alarm is obtained from impact 0 (baseline state), and the probability of detection is obtained for each damage state (impacts 1–9).

the fraction of the 24 baseline signals that were incorrectly classified. For each damage state (see figure 10), signals acquired after each impact and at different temperature (total of 20–24 signals) were analyzed and the fraction that were correctly classified was defined as the probability of detection.

Figure 12(a) shows the probability of false alarm, and figures 12(b)–(j) show the probability of detection for each of the damage states. As the number of baseline signals used for training increases, the probability of false alarm rapidly decreases from a maximum of 0.2–0 for all receivers. This happens because the classifier tends to overfit the data when given a small set of baseline references. When more baselines are available, the overfitting is less severe, however more data is still required to test the generalization of the false alarm performance. In terms of probability of detection, most sensors were capable of 100% detection of delaminations with areas larger than 2.5 cm^2 (impacts 6–9). There is one anomaly which is sensor 4B after impact 7, where the detection performance degraded to about 0.8. For a delamination area of 1.3 cm^2 (impacts 4 and 5), all receivers had a probability of detection rate above 0.9 except for receivers 5T and 5B. The reasons for this difference in performance can be explained by observing the received signals which are shown in figure 11. We can see that the signals after impact 5 are very similar to those of the baseline signals for receivers 5T and 5B. On the other hand, receivers 4 and 6 show significant changes in their amplitude and phases, which explains why they were capable of achieving a better detection performance. From a physical standpoint, the effect of a damage on the received signal depends on the position of the receiver relative to the damage area. For example, as shown in figure 7, 5T and 5B are in-line with the damage area and the transmitter, while receivers 4 and 6 are not. For delamination areas less than 1.3 cm^2 (impacts 1–3), the performance of different transducers varies significantly, for example after impact

1, and using 12 baselines for training, receiver 5T achieved only 0.05 probability of detection, while receiver 6B achieved over 0.95 probability of detection. Another common trend seen from the detection results is that the probability of detection decreases as the number of baseline training signals increases. This is due to the ‘no free lunch’ theorem where we have sacrifice detection performance if we want to enhance the false alarm performance.

These results also show that sensor fusion would give a significant improvement in probability of detection. For example, let us say we have 12 training baseline signals. If we always decide that a defect is present if at least one of the receivers decides that a damage is present, then we can always achieve a detection rate above 0.95 and a 0 false alarm rate. This can be seen in figure 12(a) where all receivers had a 0 false rate and in figure 12(b) receivers 4B and 6B had approximately 0.95 detection rate, while all the other receivers had a detection rate below 0.5.

5.4. Results using rolling baseline references

The collected experimental data does not represent a realistic environment in terms of its slow time stochasticity. To study the performance of a rolling baseline, we simulated a virtual slow time which samples signals from the collected experimental data according to a Gaussian process with a Laplacian kernel [22]. The temperature values in the virtual slow time can be mapped onto the corresponding baseline signal. The allowed slow time temperature values were confined to be between 25°C and 50°C , which is the range within which the baseline signals were recorded. However, since the virtual slow time might give a temperature where no baseline signal is available, we interpolated the feature vectors to obtain the value corresponding to the exact virtual slow time temperature.

For a given window size M , the first M signals received from the virtual slow time are used to train the classifier, and the $M + 1$ signal is used to make a defect/no defect decision. We always let the first M signals to be baseline signals, and the $M + 1$ signal represents one of the 10 damage states for the structure. For each damage state, we performed 1000 simulations and computed the probability of false positives and defect. Figure 13 shows the results for window sizes 15 and 30. The probability of false alarm is near 0.05 for all receivers when the window size is 15. The probability of false alarm goes down to 0 when the window size is increased to 30, as expected, since we now capture more variations in the virtual slow time. As for the performance in terms of probability of detection, the rolling baseline classifier follows similar trends as that of the fixed baseline classifier.

6. Conclusion

One of the prevailing challenges impeding the prompt migration of GW-SHM from laboratory settings to industry is the reliability concerns due to variations in operating and environmental conditions [26]. Our work addressed those concerns by developing a flexible and efficient classifier capable of providing high detection rates and low false alarm rates even under extremely severe environments. We demonstrated the performance of this classifier using Monte-Carlo simulations of a simplified analytical model. Furthermore, experiments have shown that this classifier is capable of perfect detection of delaminations in a composite plate with 7 cm² area, under mild variations in temperature. It would be interesting to conduct further experiments with real complex structures and under more severe environments such as large temperature fluctuations and changing loads and humidity. In addition, the sensor network used in the experiments was not optimized for detecting particular damage mode and/or reducing the sensitivity to specific environmental conditions. For example, if such a network is expected to be used in a humid environment, it would be preferable to use transducers that primarily excite symmetric modes, to minimize leakage of the waves into water.

We have also introduced the concept of modeling the effects of EOC on guided wave signals as Gaussian processes, allowing us to use rolling baseline windows determined by the decorrelation period of the covariance matrix. This overcomes the shortcomings of fixed baselines which have to account for all possible EOC to obtain a low false alarm rate. The rolling baseline window concept was demonstrated to work well with sudden damage events such as impact damage and cracks due to high cycle fatigue. The applicability of rolling window baselines for detecting slow growing cracks needs to be further studied.

ORCID iDs

Gerges Dib  <https://orcid.org/0000-0002-5500-4047>

References

- [1] Diamanti K and Soutis C 2007 Piezoelectric transducer arrangement for the inspection of large composite structures *Composites A* **38** 1121–30
- [2] Lu Y and Michaels J E 2005 A methodology for structural health monitoring with diffuse ultrasonic waves in the presence of temperature variations *Ultrasonics* **43** 717–31
- [3] Croxford A, Wilcox P, Drinkwater B and Konstantinidis G 2007 Strategies for guided-wave structural health monitoring *Proc. R. Soc. A* **463** 2961–81
- [4] Michaels J E 2008 Detection, localization and characterization of damage in plates with an *in situ* array of spatially distributed ultrasonic sensors *Smart Mater. Struct.* **17** 035035
- [5] Sohn H 2007 Effects of environmental and operational variability on structural health monitoring *Phil. Trans. A* **365** 539–60
- [6] Scholkopf B, Williamson R, Smola A, Shawe-Taylor J and Platt J 1999 Support vector method for novelty detection *Proc. 12th Int. Conf. on Neural Information Processing Systems* pp 582–8
- [7] Konstantinidis G, Drinkwater B W and Wilcox P D 2006 The temperature stability of guided wave structural health monitoring systems *Smart Mater. Struct.* **15** 967–76
- [8] Croxford A J, Moll J, Wilcox P D and Michaels J E 2010 Efficient temperature compensation strategies for guided wave structural health monitoring *Ultrasonics* **50** 517–28
- [9] Harley J and Moura J M F 2012 Scale transform signal processing for optimal ultrasonic temperature compensation *IEEE Trans. Ultrason. Ferroelectr. Freq. Control* **59** 2226–36
- [10] Salmanpour M, Sharif Khodaei Z and Aliabadi M 2016 Guided wave temperature correction methods in structural health monitoring *J. Intell. Mater. Syst. Struct.* **28** 604–18
- [11] Dib G, Koricho E, Karpenko O, Haq M, Udpa L and Udpa S S 2015 Feasibility of PZT ceramics for impact damage detection in composite structures *AIP Conf. Proc.* **1650** 1072
- [12] Dib G, Karpenko O, Koricho E, Haq M, Udpa L and Udpa S S 2015 Guided wave structural health monitoring for impact damage detection and characterization *American Society of Composites 20th Technical Conference*
- [13] Liu Y and Chattopadhyay A 2012 Low-velocity impact damage monitoring of a sandwich composite wing *J. Intell. Mater. Syst. Struct.* **24** 2074–83
- [14] Haynes C, Todd M D, Flynn E and Croxford A 2012 Statistically-based damage detection in geometrically-complex structures using ultrasonic interrogation *Struct. Health Monit.* **12** 141–52
- [15] Liu C, Harley J B, Berges M, Greve D W and Oppenheim I J 2015 Robust ultrasonic damage detection under complex environment using singular value decomposition *Ultrasonics* **58** 75–86
- [16] Mujica L E, Ruiz M, Pozo F, Rodellar J and Güemes A 2014 A structural damage detection indicator based on principal component analysis and statistical hypothesis testing *Smart Mater. Struct.* **23** 025014
- [17] Pozo F, Arruga I, Mujica L E, Ruiz M and Podivilova E 2016 Detection of structural changes through principal component analysis and multivariate statistical inference *Struct. Health Monit.* **15** 127–42
- [18] Cross E J, Manson G, Worden K and Pierce S G 2012 Features for damage detection with insensitivity to environmental and operational variations *Proc. R. Soc. A* **468** 4098–122
- [19] Putkis O and Croxford A J 2013 Continuous baseline growth and monitoring for guided wave SHM *Smart Mater. Struct.* **22** 055029

- [20] Dib G and Udpa L 2016 Design and performance of optimal detectors for guided wave structural health monitoring *Struct. Health Monit.* **15** 21–37
- [21] James G, Witten D, Hastie T and Tibshirani R 2014 *An Introduction to Statistical Learning* (New York: Springer) (<https://doi.org/10.1007/978-1-4614-7138-7>)
- [22] Rasmussen C E and Williams C K 2006 *Gaussian Processes for Machine Learning* (Cambridge: MIT Press)
- [23] Khomenko A, Karpenko O, Koricho E G, Haq M, Cloud G L and Udpa L 2016 Optical transmission scanning for damage quantification in impacted GFRP composites *Proc. SPIE* **9804** 98040R
- [24] Khomenko A, Karpenko O, Koricho E, Haq M, Cloud G L and Udpa L 2016 Theory and validation of optical transmission scanning for quantitative NDE of impact damage in GFRP composites *Composites B* **107** 182–91
- [25] Khomenko A, Karpenko O, Koricho E G, Haq M, Cloud G L and Udpa L 2017 Quantitative comparison of optical transmission scanning with conventional techniques for NDE of impact damage in GFRP composites *Composites B* **123** 92–104
- [26] Lynch J P, Farrar C R and Michaels J E 2016 Structural health monitoring: technological advances to practical implementations *Proc. IEEE* **104** 1508–12